Astronomy & Astrophysics

Cassini ISS mutual event astrometry of the mid-sized Saturnian satellites 2005–2012[*]

N. J. Cooper[1,2], C. D. Murray[1], V. Lainey[2], R. Tajeddine[3,2], M. W. Evans[3], and G. A. Williams[1]

[1] Astronomy Unit, School of Physics and Astronomy, Queen Mary University of London, Mile End Road, London, E1 4NS, UK
e-mail: n.cooper@qmul.ac.uk
[2] IMCCE, Observatoire de Paris, UMR 8028 du CNRS, UPMC, Université de Lille 1, 77 av. Denfert-Rochereau, 75014 Paris, France
[3] Department of Astronomy, Cornell University, Ithaca, NY 14853, USA

ABSTRACT

Aims. We present astrometric observations of the Saturnian satellites Mimas, Enceladus, Tethys, Dione, and Rhea from *Cassini* Imaging Science Subsystem (ISS) narrow-angle camera (NAC) images. Image sequences were designed to observe mutual occultations between these satellites.
Methods. The positions of satellite centres were estimated by fitting ellipsoidal shape models to the measured limbs of the imaged satellites. Spacecraft pointing corrections were computed using the UCAC2 star catalogue. We compare observed-minus-computed (O−C) residuals based on inter-satellite separations with those based on individual satellite positions, relative to the SAT360 and NOE-6-2012-MAIN ephemerides.
Results. We provide a total of 2303 astrometric observations, resulting in 976 pairs, the remainder consisting of observations of a single satellite. We obtain mean residuals for the individual satellite positions relative to the SAT360 ephemeris of 4.3 km in the line direction and −2.4 km in the sample direction, with standard deviations of 5.6 and 7.0 km respectively, an order of magnitude improvement in precision compared to published HST observations. We show that, by considering inter-satellite separations, uncertainties in camera pointing and spacecraft positioning along with possible biases in the individual positions of the satellites can be largely eliminated, resulting in an order-of-magnitude increase in accuracy compared to that achievable using the individual satellite positions themselves. We demonstrate how factors relating to the viewing geometry cause small biases in the individual positions of order 0.28 pixel to become systematic across the dataset as a whole and discuss options for reducing their effects. The reduced astrometric data are provided in the form of individual positions for each satellite, together with the measured positions of reference stars, in order to allow more flexibility in the processing of the observations, taking into account possible future advances in limb-fitting techniques as well as the future availability of more accurate star catalogues, such as those from the *Gaia* mission.

Key words. astrometry – occultations – planets and satellites: general – methods: observational

1. Introduction

A planned campaign of astrometric observation of the inner satellites of Saturn using the Imaging Science Subsystem (ISS) of the *Cassini* orbiter has been ongoing since Saturn orbit insertion (SOI) in July 2004. This work has been driven both by scientific objectives and as a contribution to the operational navigation effort of the *Cassini* project, with regular deliveries of observations provided to JPL for the updating of satellite orbit models throughout the mission. Recent scientific results, see for example Lainey et al. (2012), have highlighted the key role of high-resolution imaging and astrometry techniques in the solution of fundamental problems relating to the structure and dynamical evolution of planetary satellite systems. The data presented here represent a further contribution towards that wider goal.

In terms of previously published *Cassini* ISS astrometry, observations of the Jovian satellites Amalthea and Thebe using images from *Cassini*'s Jupiter fly-by were published by Cooper et al. (2006), while Tajeddine et al. (2013) published astrometry of the Saturnian satellites Mimas and Enceladus, using a variety

of ISS images, including some from the planned programme described above. Cooper et al. (2014) present astrometry of the small inner Saturnian satellites, Atlas, Prometheus, Pandora, Janus and Epimetheus using images both from the planned programme and image sequences designed to study Saturn's F ring.

The planned campaign of astrometric data collection has been divided into two parallel programmes: image sequences targeting specific individual satellites, normally identified by the label SATELLORB in the *Cassini* image sequence name, and sequences designed to capture chance occurrences of more than one satellite in the NAC field-of-view, typically with sequence name containing MUTUALEVE. The observations presented in this paper form part of the second programme.

Although we describe these observations as mutual events, we use the term somewhat more loosely to describe any partial-occultation of one satellite by another, or the occurrence of more than one satellite (without actual or partial occultation) within an image. Since all the target satellites in these images are fully resolved, we have reduced the observations using an astrometric approach based on limb-fitting, rather than the traditional photometric approach adopted for ground-based mutual phenomena for unresolved satellites, based on light curves (Thuillot et al. 2001). We described our approach in the next section.
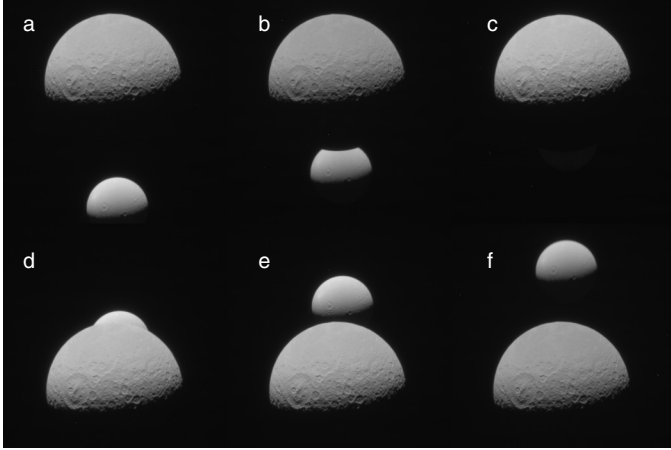

Fig. 1. A portion of selected images from sequence ISS_144RH_MUTUALEVE002_PRIME, showing Dione being occulted by Rhea. Images are **a)** N1675397022_1.IMG **b)** N1675397057_1.IMG **c)** N1675397090_1.IMG **d)** N1675397192_1.IMG **e)** N1675397226_1.IMG and **f)** N1675397261_1.IMG. The images are consecutive and taken approximately 34 s apart, except that images N1675397124_1.IMG and N1675397159_1.IMG, between **c)** and **d)** are not shown, since Dione is fully occulted for these images, as in image **c)**. Image exposure lengths are **a)** 560 ms **b)** 2000 ms **c)** 460 ms **d)** 460 ms **e)** 560 ms **f)** 2000 ms.

During the course of this work, we have also investigated potential sources of bias in the astrometric observations and discuss both their origin and possible approaches to reducing their effects.

Throughout, we use the *Cassini* ISS convention of referring to the image pixel coordinate along the *x* axis as "sample" and the *y* coordinate as "line".

2. Observations

The images in each sequence used in this work were designed to target a "primary" satellite while taking a series of images as the secondary satellite moved across the field-of-view. A selection of images from a typical sequence (ISS_144RH_MUTUALEVE002_PRIME) is provided in Fig. 1, showing the secondary satellite, in this case Dione, entering the field-of-view from the bottom of the first image (a) before being fully occulted by the primary satellite, Rhea, which remains fixed in the centre of the images. Dione then emerges from behind Rhea as the sequence progresses. The images are consecutive and approximately 34 s apart, except that two additional images in the sequence, in which Dione is still fully occulted, are not shown.

Table 1 summarises some relevant characteristics of all the image sequences used in this work. Exposure lengths varied from 60 to 2000 ms. Solar phase angles (observer-object-Sun) varied from 32.5 to 162.9 degrees, with a mean of 103.1 ± 30.5 deg, while image resolution for the primary satellite ranged from 5.2 to 25.8 km/pixel, with a mean of 13.6 ± 4.8 km/pixel. Images at the start and end of each sequence generally only contain the primary, hence there are typically more observations of each primary satellite than its corresponding secondary (Table 1). Thus, while the total number of individual observations is 2303, there are 976 pairs of observations (85% of the total) with the remaining 15% consisting of observations from

images with only one satellite present. Image size is, in all cases, 1024 by 1024 pixels.

Astrometric reduction was performed using the IDL-based *Caviar* software package, developed at Queen Mary University of London, and incorporating the NAIF SPICE library (Acton 1996) together with the UCAC2 star catalogue (Zacharias et al. 2004). Reduction consisted of a correction to the camera pointing direction for each image followed by an independent measurement of the centre-of-figure for each satellite using a limb-fitting approach. For this work, we used the Owen model for the *Cassini* ISS NAC (Owen 2003; Cooper et al. 2006) to relate the right ascension and declination of solar system objects and catalogue reference stars to their equivalent line and sample positions in each image. Tajeddine et al. (2013) developed an alternative model, which may also be used. Unlike the Owen model, the latter is more easily invertible, allowing line and sample to be more readily converted back to inertial positions, should that be required.

2.1. Camera pointing correction

For each image, the nominal camera pointing direction obtained from the SPICE "C-kernels" was corrected using an iterative minimisation of the observed-minus-computed positions of background reference stars, based on the UCAC2 catalogue. This involved firstly a manual translation of a template of predicted catalogue star positions, graphically, until approximately aligned with the imaged stars, followed by an automatic iterative search to fine-tune the alignment, typically with an accuracy of 0.1 pixel or less. The imaged star positions were computed using a centroiding technique based on the DAOPHOT method of Stetson (1987). A mean of 7.8 stars per image were detected, with a mean magnitude of 11.20 ± 1.15.

Tajeddine et al. (2013) showed how the number of detectable stars in a given image varied inversely with the size of the target satellite in the image: for very high resolution images, the satellite dominated the field-of-view, obscuring potential candidate stars for use in the pointing correction process. The mean resolution for the images used in the current work is 13.6 km/pixel. Based on the size of the largest satellite observed, Rhea, with a maximum radius of 764.30 ± 1.10 km (Thomas et al. 2007), this corresponds to an imaged diameter of about 112 pixels at zero phase angle. Thus, unlike the observations used by Tajeddine et al. (2013), which included some particularly high resolution images designed for the study of satellite surfaces, in this current work, the number of detected stars was less dependent on target size and more dependent on exposure length. Since the images used here were designed principally with astrometry in mind, exposure lengths were chosen, where possible, to balance the need to image often faint background stars against the requirements for optimum exposure of surface features.

2.2. Satellite position

The pixel coordinates of the centre-of-figure of each satellite were estimated by comparing a shape model, projected onto the image, with the position of the imaged limb itself. Shape models, in the form of ellipsoids, were extracted from the latest *Cassini* SPICE kernels and projected on to the image using the chosen reference ephemeris (SAT360) and the corrected camera pointing information. Shape models were based on Thomas et al. (2007).

Table 1. Image sequences.

Sequence	Time (UTC) [a]	Exposure (ms)	Mean phase[b] (deg)	Mean resolution[b] (km/pixel)	Primary satellite	No.[c]	Secondary satellite	No.[c]
ISS_003DI_MUTUALEVE004_PRIME	2005 Feb. 20 12:26:06.294 UTC	180	92.3	9.0	DIONE	32	RHEA	23
ISS_014TE_MUTUALEVE004_PRIME	2005 Sep. 11 21:01:14.951 UTC	100, 1500	87.9	14.4	TETHYS	33	DIONE	33
ISS_015DI_MUTUALEVE005_PRIME	2005 Sep. 16 08:15:40.484 UTC	100, 320, 380.1800	65.7	12.6	DIONE	56	TETHYS	23
ISS_016EN_MUTUALEVE002_PRIME	2005 Oct. 14 02:06:15.145 UTC	150, 260	108.5	6.8	ENCELADUS	83	TETHYS	23
ISS_016MI_MUTUALEVE007_PRIME	2005 Oct. 14 19:36:15.742 UTC	150	90.8	10.0	MIMAS	15	TETHYS	0
ISS_018TE_MUTUALEVE001_PRIME	2005 Nov. 29 04:00:09.709 UTC	150	122.2	6.6	TETHYS	4	ENCELADUS	4
ISS_018RH_MUTUALEVE011_PRIME	2005 Dec. 05 03:46:40.402 UTC	180	108.4	16.1	RHEA	38	DIONE	34
ISS_019EN_MUTUALEVE008_PRIME	2006 Jan. 02 15:30:08.579 UTC	150	97.0	15.8	ENCELADUS	17	DIONE	14
ISS_020RH_MUTUALEVE001_PRIME	2006 Jan. 27 21:22:09.716 UTC	180	123.2	18.1	RHEA	57	MIMAS	83
ISS_021RH_MUTUALEVE002_PRIME	2006 Feb. 06 04:11:37.600 UTC	180	110.0	25.8	RHEA	30	TETHYS	30
ISS_021MI_MUTUALEVE004_PRIME	2006 Feb. 11 23:18:10.437 UTC	150	101.3	22.5	MIMAS	40	TETHYS	40
ISS_021EN_MUTUALEVE009_PRIME	2006 Mar. 02 12:09:40.192 UTC	180	136.0	12.2	ENCELADUS	39	RHEA	23
ISS_021EN_MUTUALEVE005_PRIME	2006 Mar. 03 03:20:09.844 UTC	180, 220	139.0	15.4	ENCELADUS	35	DIONE	35
ISS_022EN_MUTUALEVE020_PRIME	2006 Mar. 16 08:42:10.643 UTC	120	99.5	11.3	ENCELADUS	30	TETHYS	12
ISS_022RH_MUTUALEVE009_PRIME	2006 Mar. 27 07:46:10.329 UTC	680	158.7	13.9	RHEA	10	DIONE	8
ISS_023RH_MUTUALEVE014_PRIME	2006 Apr. 14 14:55:10.507 UTC	180	130.8	20.5	RHEA	10	ENCELADUS	10
ISS_023DI_MUTUALEVE006_PRIME	2006 Apr. 17 05:29:10.052 UTC	220	120.1	20.6	DIONE	10	RHEA	10
ISS_023RH_MUTUALEVE006_PRIME	2006 May 07 02:13:09.818 UTC	820	159.8	16.1	RHEA	10	DIONE	10
ISS_024DI_MUTUALEVE002_PRIME	2006 May 14 06:43:40.157 UTC	260, 820, 1000	133.8	15.9	DIONE	31	RHEA	31
ISS_024EN_MUTUALEVE001_PRIME	2006 Jun. 06 16:01:40.167 UTC	460	162.9	25.0	ENCELADUS	0	TETHYS	9
ISS_024EN_MUTUALEVE009_PRIME	2006 Jun. 09 06:00:19.635 UTC	680	161.2	23.3	ENCELADUS	23	RHEA	0
ISS_025MI_MUTUALEVE001_PRIME	2006 Jun. 11 06:59:09.622 UTC	460	158.5	23.7	MIMAS	8	ENCELADUS	9
ISS_025RH_MUTUALEVE005_PRIME	2006 Jun. 11 08:30:39.537 UTC	560	156.5	21.9	RHEA	10	TETHYS	8
ISS_025EN_MUTUALEVE002_PRIME	2006 Jun. 13 15:00:10.227 UTC	680	159.1	24.3	ENCELADUS	8	RHEA	10
ISS_025DI_MUTUALEVE003_PRIME	2006 Jun. 14 03:38:09.998 UTC	560	159.1	22.7	DIONE	10	TETHYS	10
ISS_025RH_MUTUALEVE016_PRIME	2006 Jun. 16 10:46:09.733 UTC	560	155.2	20.3	RHEA	9	TETHYS	0
ISS_025MI_MUTUALEVE006_PRIME	2006 Jun. 21 22:58:09.851 UTC	260	148.7	20.5	MIMAS	2	TETHYS	6
ISS_025MI_MUTUALEVE007_PRIME	2006 Jul. 03 21:47:35.132 UTC	460	145.6	9.8	MIMAS	7	DIONE	10
ISS_025RH_MUTUALEVE004_PRIME	2006 Jul. 04 00:50:40.201 UTC	180	141.8	8.1	RHEA	10	ENCELADUS	6
ISS_025RH_MUTUALEVE006_PRIME	2006 Jul. 08 17:39:05.360 UTC	680	158.4	13.4	RHEA	20	TETHYS	20
ISS_047TE_MUTUALEVE004_PRIME	2007 Jun. 21 11:52:09.736 UTC	120	64.2	12.3	TETHYS	10	ENCELADUS	10
ISS_084OT_MUTGRNGAR001_PRIME	2008 Sep. 13 09:17:10.389 UTC	60	32.7	5.3	DIONE	27	ENCELADUS	19
ISS_119MI_MUTUALEVE001_PRIME	2009 Oct. 19 09:06:10.486 UTC	150	94.9	12.1	MIMAS	20	RHEA	17
ISS_119RH_MUTUALEVE001_PRIME	2009 Oct. 22 07:31:39.662 UTC	180	98.0	12.6	RHEA	20	DIONE	18
ISS_120RH_MUTUALEVE001_PRIME	2009 Oct. 26 20:22:09.847 UTC	220	113.1	11.3	RHEA	20	TETHYS	17
ISS_120EN_MUTUALEVE001_PRIME	2009 Oct. 27 01:47:09.742 UTC	150	117.3	12.7	ENCELADUS	20	TETHYS	12
ISS_121DI_MUTUALEVE001_PRIME	2009 Nov. 11 22:28:39.988 UTC	260	118.8	14.8	DIONE	20	RHEA	18
ISS_121TE_MUTUALEVE001_PRIME	2009 Nov. 11 23:25:09.968 UTC	220	115.4	14.1	TETHYS	20	ENCELADUS	17
ISS_121EN_MUTUALEVE001_PRIME	2009 Nov. 15 12:15:09.846 UTC	120	115.2	13.7	ENCELADUS	20	RHEA	20
ISS_121RH_MUTUALEVE002_PRIME	2009 Nov. 26 15:18:09.980 UTC	180	103.6	10.5	RHEA	20	TETHYS	18
ISS_121DI_MUTUALEVE002_PRIME	2009 Nov. 28 13:52:39.787 UTC	180	109.5	13.1	DIONE	20	TETHYS	17
ISS_122RH_MUTUALEVE003_PRIME	2009 Dec. 01 21:38:09.761 UTC	150	107.3	12.3	RHEA	20	ENCELADUS	16
ISS_127DI_MUTUALEVE002_PRIME	2010 Feb. 24 06:53:09.886 UTC	150	116.6	12.2	DIONE	22	ENCELADUS	21
ISS_128DI_MUTUALEVE002_PRIME	2010 Mar. 23 12:11:09.963 UTC	460, 680, 2000	87.4	7.2	DIONE	27	MIMAS	16
ISS_128DI_MUTUALEVE003_PRIME	2010 Mar. 26 19:03:09.955 UTC	460, 680, 2000	89.9	11.7	DIONE	27	TETHYS	26
ISS_135DI_MUTUALEVE001_PRIME	2010 Jul. 27 00:15:39.574 UTC	150, 460, 560, 2000	78.5	6.6	DIONE	23	RHEA	21
ISS_141DI_MUTUALEVE002_PRIME	2010 Dec. 06 06:33:09.863 UTC	320, 460, 1800	75.2	13.1	DIONE	75	TETHYS	75
ISS_143RH_MUTUALEVE003_PRIME	2011 Jan. 20 18:18:09.919 UTC	560, 1000, 2000	99.6	17.0	RHEA	32	DIONE	28
ISS_144RH_MUTUALEVE002_PRIME	2011 Feb. 03 03:12:09.672 UTC	460, 560, 2000	75.2	7.1	RHEA	27	DIONE	17
ISS_147RH_MUTUALEVE006_PRIME	2011 Apr. 25 19:25:40.172 UTC	320, 380, 1500	66.9	13.3	RHEA	30	ENCELADUS	33
ISS_150DI_MUTUALEVE006_PRIME	2011 Jul. 18 01:19:09.625 UTC	560, 680, 2000	37.3	13.1	DIONE	24	RHEA	13
ISS_158RH_MUTUALEVE001_PRIME	2011 Dec. 07 04:50:10.103 UTC	460, 680, 2000	72.4	11.7	RHEA	30	DIONE	30
ISS_162TE_MUTUALEVE002_PRIME	2012 Mar. 14 01:22:39.857 UTC	150, 180, 820	51.7	10.1	TETHYS	29	DIONE	20

Notes. [a] Mid-time for first image in sequence. [b] For primary satellite. [c] Zero indicates limb-fitting failed.

Each imaged limb position was estimated by computing the maximum of the numerical derivative within a three-by-three array of pixels centred at a given pixel location. Detected limb points greater than two pixels away from the predicted limb position, based on the reference ellipsoid, were rejected. Different values were tested. Given that the camera pointing correction was applied before the limb-finding/fitting, the measured limb positions were considered unlikely to be more than two pixels from their predicted locations based on the best available shape models. Using a progressively smaller value than 2.0 pixel reduced the scatter in the observed residuals (next section), but artificially drove the estimated limb points towards their predicted locations. It was considered more desirable to avoid this, at the expense of more random scatter in the residuals.

An iterative fitting procedure was used to find the optimum alignment of the position of the limb (based on the shape model) with the imaged limb positions. The observed position of the centre-of-figure was then computed by correcting the predicted position by the mean shift required to align, optimally, the measured and predicted limbs. Five ellipse parameters could potentially be fitted. However, the ellipsoid projection fixes the size of the ellipsoid, while its orientation is fixed by the satellite's known orientation to the order of 0.1 degree (Archinal et al. 2011) and the camera's twist angle (known to order of 60 μrad (Porco et el. 2004) and 90 μrad (Tajeddine et al. 2013), leaving the ellipse's centre to be fitted only.

The measured pixel coordinates (line versus sample) for each satellite are shown in Fig. 2.

2.3. Reduced data

To allow more flexibility in the use of the reduced data, we provide separate positions for each satellite, rather than inter-satellite coordinates, particularly given that some images (~15% of the total) contain only one satellite.

Table 2. Sample of *Cassini* ISS observations.

Image ID	Mid-time (UTC)	α_c (deg)	δ_c (deg)	TWIST (deg)	Line[a] (px)	Sample[a] (px)	α (deg)	δ (deg)	Body
N1487595425	2005 Feb. 20 12:30:38.277	27.296799	−6.438903	178.585994	595.83	591.92	27.268304	−6.467161	DIONE
N1487595459	2005 Feb. 20 12:31:12.277	27.289024	−6.438771	178.630998	595.78	591.47	27.260708	−6.467036	DIONE
N1487595459	2005 Feb. 20 12:31:12.277	27.289024	−6.438771	178.630998	621.95	994.47	27.121289	−6.472685	RHEA
N1487595493	2005 Feb. 20 12:31:46.276	27.281160	−6.438414	178.595788	596.02	590.78	27.253062	−6.466749	DIONE
N1487595493	2005 Feb. 20 12:31:46.276	27.281160	−6.438414	178.595788	622.42	947.46	27.129638	−6.472789	RHEA

Notes. Columns α_c, δ_c and TWIST refer to the right ascension, declination and twist angle of the camera's pointing vector in the International Celestial Reference Frame (ICRF), while α and δ are the right ascension and declination in the ICRF for the body listed in the far right-hand column. Relative to the SAT360 ephemeris, considering all the individual positions together, we obtain a precision of 0.34 pixels in line and 0.41 in sample. [a] The origin of the line, sample coordinate system is at the top left of the image with line, y, increasing downwards and sample, x, to the right. Image size is 1024 by 1024 pixels. The full table is available from the CDS.
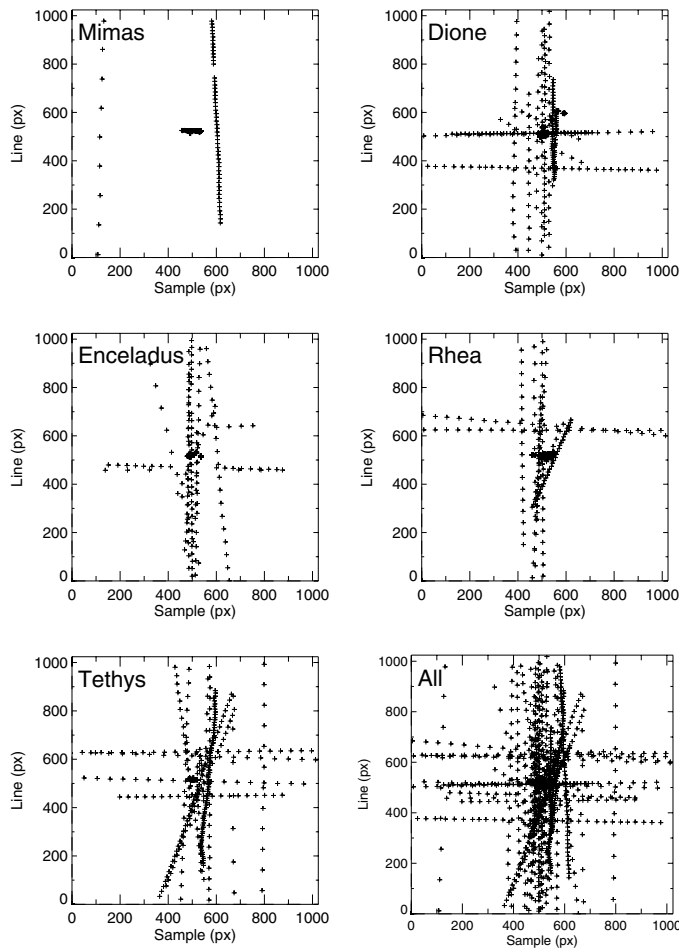
Fig. 2. Observed image positions of satellite centres, line versus sample. Image sizes are 1024 by 1024 pixel.

Also, following Cooper et al. (2006); Tajeddine et al. (2013), in addition to providing the measured satellite positions in right ascension and declination (α, δ) in the International Celestial Reference Frame (ICRF), we provide their measured pixel coordinates and camera pointing directions, so that either of these sets of measurement can easily be re-estimated independently at some future date, if required. This would, for example, allow the camera pointing corrections to be updated using improved star catalogues, such as those soon to become available from the *Gaia* mission, or for the astrometric positions themselves to

be re-estimated independently of the pointing corrections, if advances in limb measurement or centre-finding became available (see also the section on Sources of Error). Alternatively, a different NAC camera distortion model, such as that developed by Tajeddine et al. (2013), could also be used.

The complete set of reduced data is available at the CDS. A small section of the table showing the satellite positions is reproduced in Table 2. Computed star positions (Table 5) are only available electronically at the CDS.

3. Analysis of residuals

In this work, we compared observed minus computed (O−C) residuals relative to two different ephemerides: JPL's SAT360 ephemeris, based on a fit to Earth-based, Pioneer, Voyager, HST and *Cassini* data to the end of 2013, and NOE-6-2012-MAIN, created by IMCCE Paris based on a fit to Earth-based and spacecraft data from 1886–2012. In both cases, these are post-fit residuals, since the orbit models on which both these ephemerides are based included the observations presented here. However, SAT360 was generated based on corrected astrometry, which included a constant sample and line bias due to camera pointing plus additional corrections for the satellite-dependent phase biases (Jacobson, priv. comm.).

In Fig. 3, we show O−C residuals relative to the SAT360 ephemeris for the 976 pairs of observations. Figure 3a shows the residuals, line versus sample, for each individual observation, computed using the absolute satellite positions, while Fig. 3b shows the equivalent residuals based on the separation between the primary and secondary satellite in each image. The mean line and sample residuals for the absolute positions in Fig. 3a are 0.27 and −0.11 pixel respectively, with σ values of 0.34 and 0.37 pixel, while for the inter-satellite separations (Fig. 3b), we obtain an order-of-magnitude improvement in accuracy, with means of −0.03 and −0.01 pixel respectively and σ values of 0.29 and 0.26 respectively. The equivalent mean residual values across all absolute positions (2303 values) in km are 4.3 km (line) and −2.4 km (sample), with σ values of 5.6 and 7.0 km, respectively. By comparison, French et al. (2006) obtained typical uncertainties at Saturn of 80 km and 120 km respectively, using the Planetary Camera and the Wide Field Planetary Camera 2 of the *Hubble* Space Telescope.

We discuss these results further in the following section.

Line and sample residuals for each individual satellite (absolute positions) are plotted as a function of time relative to the SAT360 ephemeris in Fig. 4 and as line versus sample in Fig. 5.
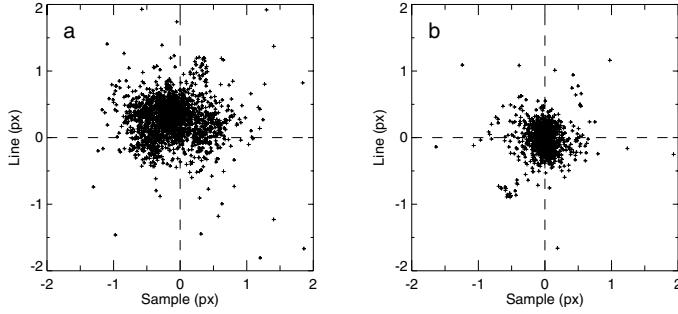
Fig. 3. Comparison between O−C residuals **a)** based on absolute positions and **b)** those based on inter-satellite differences, plotted as line residual versus sample residual relative to the JPL SAT360 ephemeris. All satellites are shown. Units are NAC pixels.
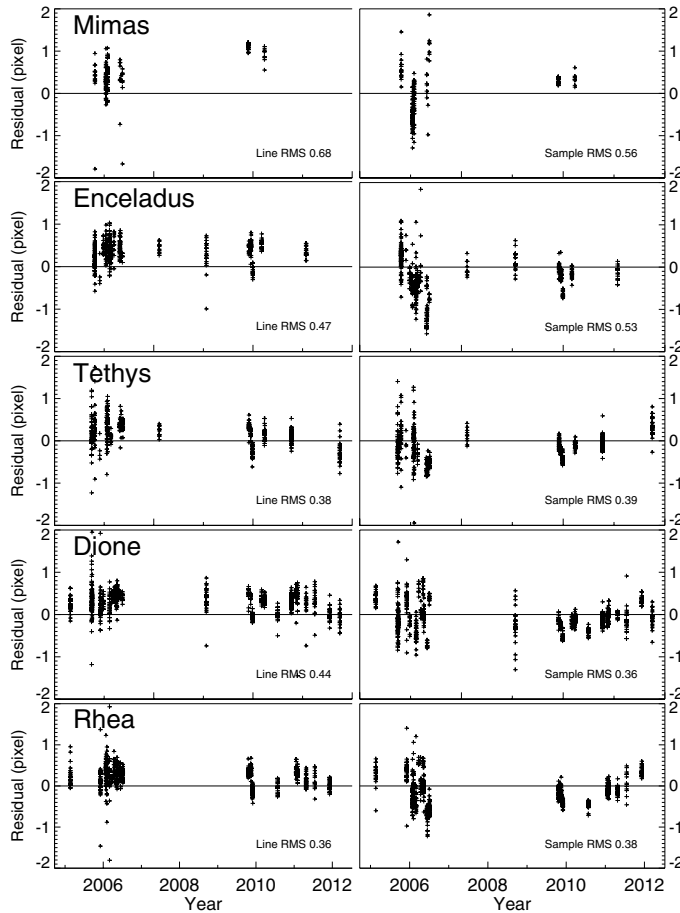

Fig. 4. O−C residuals for each satellite, using absolute positions, plotted versus time relative to the JPL SAT360 ephemeris. For each satellite, line residuals are plotted on the left, and sample on the right. Units are NAC pixels.

Fig. 5. O−C residuals for each satellite, using absolute positions, relative to the JPL SAT360 ephemeris, plotted as line residual versus sample residual. Units are NAC pixels.

Table 3. Mean values of residuals in pixels relative to the JPL SAT360 ephemeris, including standard deviations.

	Line	σ_{line}	Sample	σ_{sample}
Mimas	0.44	0.52	−0.04	0.56
Enceladus	0.35	0.32	−0.24	0.47
Tethys	0.16	0.35	−0.13	0.36
Dione	0.30	0.32	−0.07	0.36
Rhea	0.24	0.28	−0.11	0.37
All	0.28	0.34	−0.12	0.41
All (inter)[a]	−0.03	0.29	−0.01	0.26

Notes. [a] Using inter-satellite separations between pairs of satellites within a given image.

4. Sources of error

Tajeddine et al. (2013) give a detailed description of the sources of uncertainty in the astrometric reduction of *Cassini* ISS data. Here we focus on possible systematic errors in the absolute positions, that might give rise to the non-zero means of several tenths of a pixel, mentioned in the previous section. Although these biases are small in comparison to the typical accuracy achieved with earth-based astrometry (French et al. 2006), and we have seen in the previous section that they can be largely eliminated

by measuring inter-satellite separations, it is clearly desirable to understand their origin.

As noted previously, Figs. 3–5 indicate a non-zero mean of 0.28 pixels in the line residuals across all five satellites. This is also clear quantitatively in Tables 3 and 4 where we show mean values relative to two different ephemerides. The mean line residuals are consistently positive, although there is some variation in the magnitude of the mean, both between satellites, and also depending on the reference ephemeris used. The largest positive mean values occur in the line residuals for Mimas and Enceladus, based on either of the reference ephemerides

Table 4. Mean values of residuals in pixels relative to the IMCCE NOE–6-2012-MAIN ephemeris, including standard deviations.

	Line	σ_{line}	Sample	σ_{sample}
Mimas	0.55	0.57	–0.25	1.19
Enceladus	0.32	0.42	–0.30	0.40
Tethys	0.18	0.47	0.01	0.52
Dione	0.19	0.38	–0.04	0.35
Rhea	0.26	0.31	–0.08	0.39
All	0.25	0.42	–0.10	0.51
All (inter)[a]	0.04	0.41	–0.08	0.30

Notes. [a] Using inter-satellite separations between pairs of satellites within a given image.

(SAT360 and NOE-6-2012-MAIN). Given that these are post-fit residuals, the implication is either that there is a missing or poorly-determined dynamical component in the models used to generate both ephemerides, or that there is a systematic bias in the measurements, or a combination of both. Since all five satellites show a positive mean at some level, an inadequacy in the modelling would have to affect all five satellites in the same direction, which seems less likely than a systematic bias in the measurements. Also, any inadequately modelled component in the dynamics would give rise to a bias in both absolute and relative positions, which is not observed.

Some measurement bias is inevitable because the phase angle is never precisely zero in practice, so that imaged limbs are always one-sided, with the terminator forming what remains of the boundary of the satellite image. This is true for all resolved observations based on limb measurement. Tajeddine et al. (2013) also found a positive bias in the residuals for Mimas and Enceladus in the direction towards the Sun, with a significantly larger bias for Mimas than Enceladus. They put forward two possible explanations: (1) that the greater level of cratering on Mimas may distort the limb and (2) that the dimensions of Mimas could be larger than those based on the shape model of Thomas et al. (2007). However, in the data presented here, this effect is systematic across all the observations for five different satellites, implying that some common geometric characteristic of the dataset as a whole is the key contributory factor: if the limbs had randomly distributed phases and illumination directions, this effect would not be systematic. A clue that such a common geometric characteristic exists is evident from Fig. 2, showing how the measurements are distributed dominantly along the line axis.

We investigated this further using synthetically-generated images, whose centre-of-figure is known in advance. Sequences of images were generated, using the *Mathematica* software package (Wolfram Research Inc. 2012) for different illumination directions and phase angles, in order to assess possible measurement bias as a function of these parameters. In Figs. 6 and 7, we show using these synthetic images how the limb-fitting algorithm does indeed generate a bias in the computed centre-of-figure that varies as a function of phase angle and illumination direction. The maximum size of the observed bias is more than 1.5 pixel, which is almost an order of magnitude larger than the mean values we obtain for the real images. This discrepancy arises because the illumination model used to generate the synthetic images is not a realistic photometric match for the real images. Thus this comparison is illustrative only and serves purely to demonstrate how a bias can arise and how it may change according to the imaging geometry.
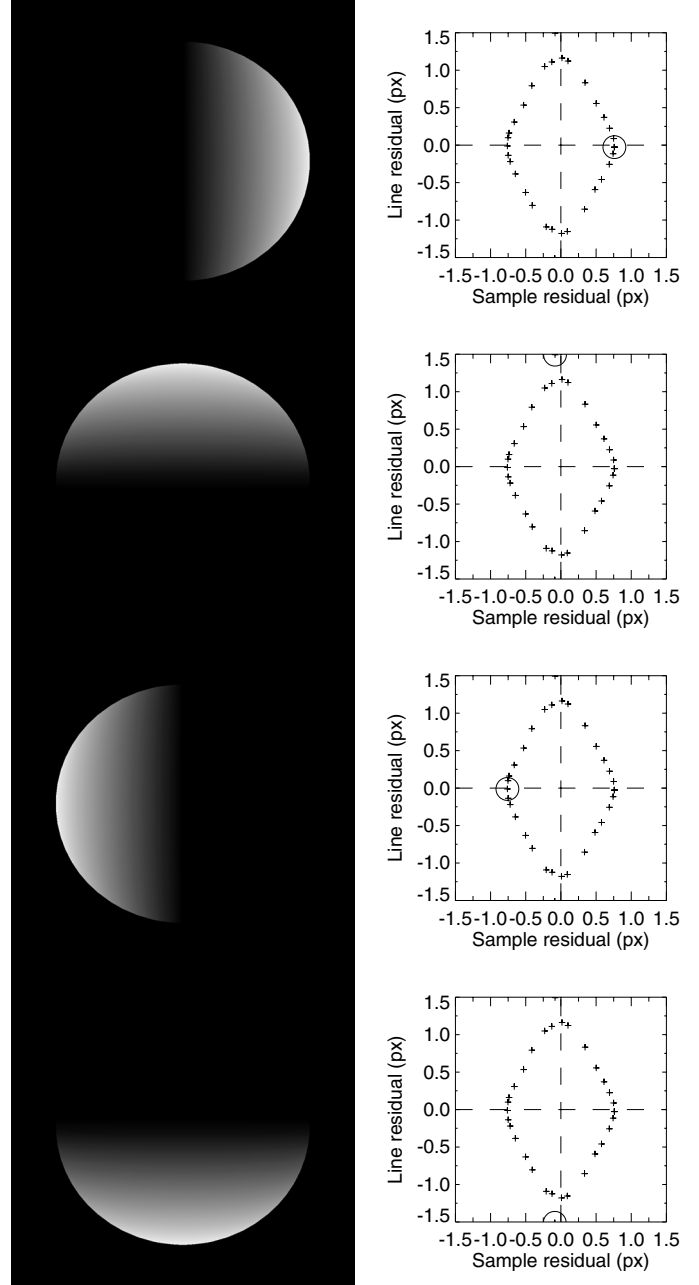
Fig. 6. Synthetic images for different illumination directions, showing O−C residuals in pixel (*right*) for centre-of figure positions measured by limb-fitting the images shown left. The bias is always in the illumination direction. All points in the right-hand displays are the same, with the particular O−C residual values corresponding to each of the four images represented by the small circles (directions are, *from top to bottom*, 0 deg, 90 deg, 180 deg, 270 deg).

Returning to the question of why this appears as a systematic effect in the real data, in Fig. 8a, we plot the variation of phase angle across the entire set of real images. This shows clearly that phase angles across all the observations are clustered around 90−100 degrees (see also the mean phase values listed in Table 1). Furthermore, Fig. 8b shows that the Sun directions are also preferentially distributed along the positive line direction. We conclude therefore that the combination of these two geometrical characteristics of the images accounts for the systematically positive mean values in the absolute positions: from the synthetic tests, the maximum possible bias occurs at ∼90 degree
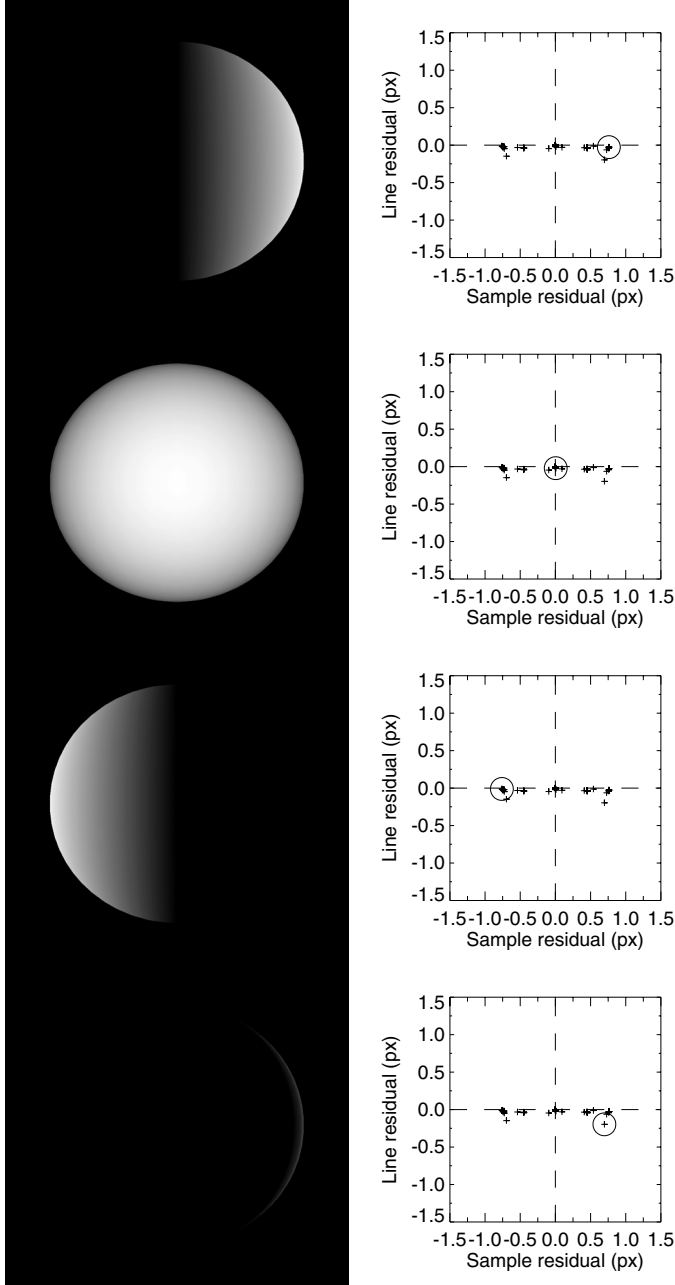
Fig. 7. Synthetic images for different phase angles, showing O−C residuals in pixel (*right*) for centre-of figure positions measured by limb-fitting the images shown left. The maximum bias occurs for 90 degree phase and is zero for zero phase. All points in the right-hand displays are the same, with the particular O−C residual values corresponding to each of the four images represented by the small circles (phase angles are, *from top to bottom*, +90 deg, 0 deg, −90 deg, 180 deg).

Fig. 8. Distribution of **a)** satellite phase angles and **b)** Sun directions for the *Cassini* images used in this work. Sun directions are resolved into line and sample directions within each image.

phase angle, and the common alignment of the limbs in the real images in the positive line direction then accounts for the appearance of a systematic positive bias in that direction across all the absolute positions.

5. Discussion and conclusions

A particular advantage of all mutual event observations, using either ground-based or spacecraft imaging, is that image-dependent errors cancel when computing the separation between two satellites in the same image, leading to a potentially significant increase in accuracy. This type of observation is also useful when no suitable reference stars are detectable within a given image. Although we did not foresee the tendency of the limb-fitting method to introduce a bias in the absolute positions of satellite centres-of-figure in the direction of the limb (i.e. in the Sun direction), we have shown that this also cancels when computing inter-satellite separations because the magnitude and direction of the bias turns out to be dependent on phase angle and Sun direction, and these two quantities, like the camera pointing direction, are also effectively constant for a given image.

On the other hand, a single measurement of the separation between two satellites necessarily contains less information than the individual absolute positions combined. Thus there is an inevitable trade-off in information content versus accuracy, depending on which of the two approaches to data reduction is used. This is one reason why we have chosen to provide the raw data in terms of the absolute positions, in order to give the reader the option to use either approach.

As described previously, investigation showed that Sun orientations (and phase angles) are preferentially distributed in one direction across the dataset as a whole and thus the bias, rather than being randomly distributed, has a preferred orientation in that direction (the positive line direction). This is an unintended consequence of the particular observing geometry of the image sequences, *Cassini* Project standard operational practice and the habits of the imaging sequence designers.

Given that there may be circumstances where it is more desirable to make use of the greater information content of the absolute positions, the question arises as to what can be done either to correct such biases, or to minimise their occurrence in the first instance. We have considered four approaches: (a) correcting an existing bias using information derived from synthetic images, (b) correcting an existing bias by subtracting mean values derived for each satellite, (c) changing the observation strategy to prevent the bias from occurring systematically in one direction and (d) improving the performance of the limb-measuring technique to try to reduce the magnitude of any bias.

Firstly, considering (a), the synthetic images have provided a useful way of evaluating how the measured centre-of-figure based on limb-fitting behaves as a function of phase angle and illumination direction. Thus, in principle, a table of corrections could be generated from these synthetic images, corrections which could then be applied to the real observations in order to remove any potential bias generated in the limb-fitting. However, as noted previously, the magnitude of the bias we currently obtain from the synthetic images is much larger than any effect we see in the real observations, so this approach would only be viable if a way could be found to model the limb profiles to give

a satisfactory photometric representation of the profiles obtained from the real images. Although a photometric approach is routinely used for ground-based observations of mutual phenomena for unresolved bodies (see for example Noyelles et al. 2003; Arlot & Thuillot 2008), to our knowledge this has not been attempted for observations of resolved satellites, where centre-of-figure measurements are based on limb-fitting. Clearly, with an observed mean bias of less than 0.2 pixel for some satellites, any such correction process would have to be precise enough so as not to risk introducing a bias in a different direction. This will be the subject of further work.

In principle, biases in the absolute positions could also be corrected by applying a global correction for each satellite, prior to orbit modelling, based on the computed mean values of the O−C residuals relative to a suitable reference ephemeris. However, clearly this can only be justified if there is sufficient confidence that the mean values do not represent genuine dynamical effects.

A different approach to observing the mutual events with the aim of randomising the Sun directions would potentially reduce the tendency of the bias to be systematic in one direction. However this would only randomise the direction of the bias across the dataset as a whole and would not reduce its magnitude in a given image. Also any such modification of the observing strategy would still need to satisfy spacecraft flight rules.

A possible fourth approach would be to improve the performance of the limb-measurement algorithms in order to minimise the magnitude of any possible bias in a given image. Approaches which we have investigated so far have included the application of a gaussian to the derivative in order to estimate the limb position to sub-pixel precision, the use of other edge detection algorithms, such as the Canny algorithm (Canny 1986), and the interpolation of the input images to produce finer spatial sampling, before limb fitting. Preliminary investigations have shown that all these approaches, to a greater or lesser degree, can provide some improvement in the overall precision of the data, but do not significantly increase the accuracy.

Although these are small effects, which we already have seen can be largely eliminated by measuring the separations between pairs of satellites in each mutual event image, further investigation would still be advantageous, particularly given the need for ever greater astrometric accuracy based on current scientific goals.

References

Acton, C. H. 1996, Planet. Space Sci., 44, 65
Archinal, B. A., A'Hearn, M. F., Bowell, E., et al. 2011, CeMDA, 109, 101
Arlot, J. E., & Thuillot, W. 2008, A&A, 485, 293
Canny, J. 1986, IEEE Trans. Pattern Analysis and Machine Intelligence, 8, 679
Cooper, N. J., Murray, C. D., Porco, C. C., & Spitale, J. N. 2006, Icarus, 181, 223
Cooper, N. J., Renner, S., Murray, C. D., & Evans, M. W. 2014, AJ, submitted
French, R. G., McGhee, C. A., Frey, M., et al. 2006, PASP, 118, 246
Lainey, V., Karatekin, O., Desmars, J., et al. 2012, ApJ, 752, 14
Noyelles, B., Vienne, A., & Descamps, P. 2003, A&A, 401, 1159
Owen, W. M. Jr. 2003, JPL IOM 312.E-2003
Porco, C. C., West, R. A., Squyres, S., et al. 2004, Space Sci. Rev., 115, 363
Stetson, P. B. 1987, PASP, 99, 191
Tajeddine, R., Cooper, N. J., Lainey, V., Charnoz, S., & Murray, C. D. 2013, A&A, 551, A129
Thomas, P. C., Burns, J. A., Helfenstein, P., et al. 2007, Icarus, 190, 573
Thuillot, W., Arlot, J. E., Ruatti, C., et al. 2001, A&A, 371, 343
Wolfram Research, Inc., Mathematica, Version 9.0, Champaign, IL (2012)
Zacharias, N., Urban, S. E., Zacharias, M. I., et al. 2004, AJ, 127, 3043